RSC Advances

PAPER

View Article Online
View Journal | View Issue

Cite this: *RSC Adv.*, 2026, **16**, 17869

Development of a molecularly imprinted electrochemical sensor based on (Cu-BTC)-MOF and graphene composite for highly sensitive and selective chloramphenicol detection

Ni Xiang,[a] Suijian Qi[a] and Jinhua Piao *[ab]

Received 29th December 2025
Accepted 16th March 2026

DOI: 10.1039/d5ra10071b

rsc.li/rsc-advances

A highly selective molecularly imprinted electrochemical sensor was constructed for chloramphenicol (CAP) detection based on a copper-benzenetricarboxylic acid metal–organic framework (Cu-BTC)-MOF)/graphene (Gr) composite and poly(*o*-phenylenediamine) (*o*-PD) molecularly imprinted polymer (MIP). The (Cu-BTC)-MOF exhibits extremely high porosity, adjustable pore size, a large specific surface area, and highly dispersed unsaturated metal sites. These properties enable it to provide active centers, guide the orderly growth of MIPs, or anchor functional groups, all of which are beneficial for improving the detection performance and stability of the sensor. Graphene, as a support substrate for (Cu-BTC)-MOF, can significantly improve the dispersion, structural stability and conductivity of (Cu-BTC)-MOF. *o*-PD serves as a functional monomer with two amino active sites, which enable hydrogen bonding or electrostatic interactions with the functional groups (such as carboxyl or hydroxyl) of target molecules, thus enhancing template-specific recognition. The aromatic ring of *o*-PD facilitates π–π stacking and can broaden the recognition scope. The fabricated sensor exhibits a wide detection range of 0.1 to 120 μM, a low detection limit of 0.05 μM and high sensitivity of 0.186 μA μM^{-1}. Furthermore, it also demonstrated good selectivity, reproducibility and high stability. Moreover, the proposed molecularly imprinted electrochemical sensor was successfully used to assess the chloramphenicol content in real food samples. Therefore, this work presents a simple and efficient strategy for detecting chloramphenicol, which could aid in applying molecularly imprinted electrochemical sensors across various detection scenarios.

1 Introduction

Chloramphenicol (CAP), as a broad-spectrum antibiotic, can inhibit bacterial protein biosynthesis and effectively kills or suppresses various cocci, bacilli, and spirochetes and so on.[1,2] Therefore, CAP is widely utilized in disease prevention and treatment as well as in animal husbandry. However, its misuse can lead to detectable residues in meat, eggs, milk, and other poultry products, posing significant health risks to consumers. The overuse of CAP leads to serious health issues, including aplastic anemia, leukemia, gray baby syndrome, liver function abnormalities and hematologic system disorders. Additionally, it also carries genetic toxicity and carcinogenic risks.[2–4] Therefore, international organizations and individual countries or regions enforce highly stringent standards for chloramphenicol residues in food products. For example, the European Union has stipulated that the maximum allowable concentration of chloramphenicol in food cannot exceed 0.3 μg kg^{-1}. Countries such as China, the United States and Japan have also established regulations prohibiting the CAP residues, specifying that it must not be detectable.[5] Thus, developing sensitive, precise and rapid CAP detection methods is of great significance in aspects such as food safety, clinical medicine, environmental protection. Traditional methods for detecting CAP mainly include gas chromatography,[6] gas chromatography-tandem mass spectrometry,[7] high-performance liquid chromatography-mass spectrometry[8] and so on. However, some disadvantages, such as high equipment costs, strict operational requirements, the need for specialized personnel, prolonged detection times and complicated pre-treatment procedure, have limited their widespread application. Electrochemical detection methods, especially electrochemical sensors, have attracted extensive attention for detecting CAP due to high sensitivity and selectivity, low cost, simple operation, fast detection speed and simple pretreatment.[9–12] For example, Liu *et al.* constructed an electrochemical aptasensor utilizing reduced graphene oxide and silver nanoparticles for CAP detection, demonstrating an

---

[a] *School of Food Science and Engineering, South China University of Technology, Guangzhou 510641, China. E-mail: jhpiao@scut.edu.cn*

[b] *Guangdong Provincial Key Laboratory of Green Processing of Natural Products and Product Safety, Guangzhou 510641, China*

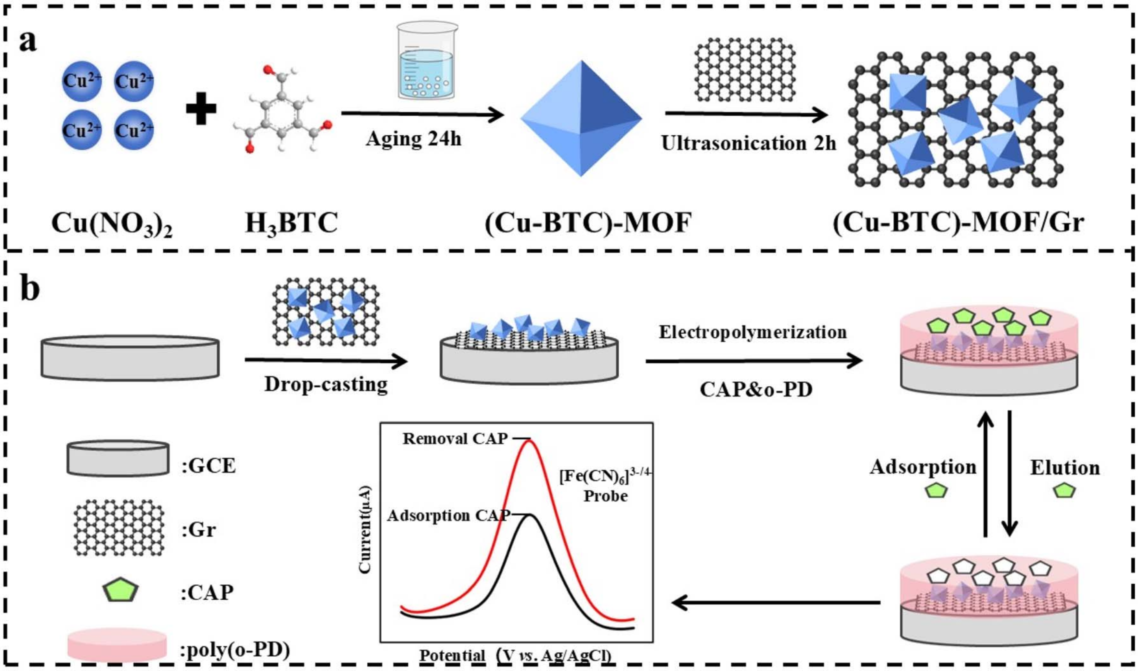

Scheme 1 (a) Illustration of the synthesis process of (Cu-BTC)-MOF/Gr composite, (b) schematic illustration of the construction of the MIP/(Cu-BTC)-MOF/Gr/GCE chlorampheniol sensor.

excellent detection range from 0.01–35 μM with an ultra-low detection limit of 2 nM.[12] Compared to other types of sensors, molecularly imprinted electrochemical sensor (MIES) is an ideal alternative analytical technique for ultrasensitive and rapid detection of chloramphenicol, but their selectivity and sensitivity were still not satisfactory. Meanwhile, the molecular imprinted polymers (MIPs) prepared with conventional methods had less effective binding sites as many binding sites were buried in polymeric matrix, which limits its development. By rational designing the MIP layer and electrode interface, this type of sensor can be widely applied in environmental monitoring, food safety, medical diagnostics, and other fields.[12–14]

As the core component of the MIES, the functional monomer can form a pre-assembled complex through specific interactions with the template molecule, such as hydrogen bonds, electrostatic interactions, hydrophobic interactions. This process enables the formation of high selective recognition sites for the template molecule following polymerization.[15–17] *o*-Phenylenediamine (*o*-PD) is a widely used functional monomer in molecular imprinting. Its molecular structure features two amino active sites and a benzene ring, enabling hydrogen bonding or electrostatic interactions with functional groups of target molecules, thereby enhancing template-specific recognition. The aromatic ring facilitates π–π stacking with aromatic compounds (*e.g.*, polycyclic aromatic hydrocarbons and pharmaceutical molecules), broadening the recognition scope.[18,19] Ding *et al.* developed a MIES based on tungsten oxide (WO_3) and molybdenum dioxide (MoO_2) for imidacloprid detection, employing *o*-PD as the functional monomer. The sensor exhibited a linear detection range of 0.5–70 μM and a limit of detection (LOD) of 0.1 μM.[20] Owing to its versatility, stability, and processability, *o*-PD has become a highly competitive functional monomer choice for molecularly imprinted sensors. Hence, we consider that it is possible to develop a molecularly imprinted electrochemical sensor using *o*-PD as functional monomer.

Metal–organic frameworks (MOFs) materials, such as Fe-MOF, Ce-MOF, and Cu-MOF have emerged as promising materials for electrode surface modification in catalysis[21–24] and biosensing owing to their structural diversity, ultrahigh specific surface area, high porosity, tunable pore size, and excellent physical/chemical stability.[25–29] Among various MOF candidates, the copper-benzenetricarboxylic acid metal–organic framework (Cu-BTC)-MOF (also known as HKUST-1) stands out as an optimal platform for electrochemical sensors because of its large specific surface area, excellent porous structure, good stability, high catalytic efficiency, mild synthesis conditions, and low cost.[27] The unsaturated Cu^{2+} sites in the (Cu-BTC)-MOF framework can also serve as catalytic active centers for catalytic reactions such as oxidation and cycloaddition. However, its inherent low conductivity significantly affects electron transfer kinetics, which severely limits its application in electrochemical sensors. To overcome above-mentioned shortcomings, coupling (Cu-BTC)-MOF with other conductive materials has proven to be an effective solution.[30–33] Graphene (Gr) has been extensively utilized in electrochemical sensors due to its high specific surface area, excellent stability, and superior electrical conductivity.[34–36] Thus, it is expected that combining (Cu-BTC)-MOF with graphene will develop a new composite material which can improve the activity and stability of electrochemical sensors.

In this work, a highly sensitive and selective molecularly imprinted electrochemical sensor based on a (Cu-BTC)-MOF and graphene ((Cu-BTC)-MOF/Gr) composite nanomaterial was developed for chloramphenicol detection. In this sensor, the as-prepared (Cu-BTC)-MOF/Gr composite was used as substrate, guiding the orderly growth of MIP. *o*-PD was used as functional monomer for MIP synthesis. The amino group and benzene ring in the molecular structure of *o*-PD can enhance template-specific recognition and broaden the recognition scope through hydrogen bonding, electrostatic interactions, and π–π stacking reaction, thereby enhancing specificity of the sensor. The designed sensor was immobilized on a glassy carbon electrode (GCE). The preparation process of the (Cu-BTC)-MOF/Gr composite (a) and the fabrication procedure of the MIP/(Cu-BTC)-MOF/Gr/GCE CAP molecularly imprinted electrochemical sensor (b) were shown in Scheme 1. In the experiment, an octahedral (Cu-BTC)-MOF with high specific surface area and porosity was synthesized using a liquid-phase method. The (Cu-BTC)-MOF was then mixed with Gr to obtain the (Cu-BTC)-MOF/Gr composite. The prepared (Cu-BTC)-MOF/Gr composite was decorated onto a GCE substrate *via* a drop-coating method to fabricate the (Cu-BTC)-MOF/Gr/GCE modified electrode. Subsequently, a molecularly imprinted film was formed on this electrode *via* electropolymerization, using *o*-PD as the functional monomer. In the designed MIP/(Cu-BTC)-MOF/Gr/GCE molecularly imprinted sensor, the large specific surface area and excellent conductivity of the (Cu-BTC)-MOF/Gr composite increase more MIP sites, higher binding capacity and improve electron transfer performance in the modified electrode. Meanwhile, the *o*-PD functional monomer, featuring amino active sites and benzene rings, contributes to the specific recognition of chloramphenicol molecular templates, ultimately improving the selectivity of the sensor. Overall, the sensor based on (Cu-BTC)-MOF/Gr composite and *o*-PD functional monomer indicates that the rational design of nanocomposites with high specific surface area and conductivity, combined with the selection of suitable functional monomers, can significantly enhance the detection performance and selectivity of molecularly imprinted sensors. It provides valuable insights for designing a highly sensitive and selective molecularly imprinted electrochemical sensor.

2 Experimental

2.1 Materials and chemicals

Copper nitrate trihydrate ($Cu(NO_3)_2 \cdot 3H_2O$, 99%), 1,3,5-benzenetricarboxylic acid (H_3BTC, 98%), polyvinylpyrrolidone K30 (PVP-K30, >99%), high purity graphene powder (Gr, 99%), *o*-phenylenediamine (*o*-PD, 98%), chitosan (CHIT, 90%), chloramphenicol (CAP, 98%), oxytetracycline (OTC, ≥98%), gentamicin sulfate (GM, 98%), streptomycin sulfate (SS, 98%), neomycin sulfate (NS, 97%), tetracycline (TC, 98%) were purchased from Shanghai Macklin Biochemical Co., Ltd (China). Potassium chloride (KCl, 99.5%), potassium hexacyanoferrate ($K_3[Fe(CN)_6]$, 99.5%), potassium ferrocyanide trihydrate ($K_4[Fe(CN)_6] \cdot 3H_2O$, 99%), sodium phosphate dibasic (Na_2HPO_4, 99%), sodium phosphate monobasic dihydrate ($NaH_2PO_4 \cdot 2H_2O$, 99%), methanol (MeOH, ≥99.9%), ethanol (EtOH, ≥99.7%), acetic acid glacial (HAc, ≥99.5%), isopropyl alcohol (IPA, ≥99.5%) were obtained from Shanghai Aladdin Bio-chem Technology Co., Ltd (China). Milk came from Yili Industrial Group Co., Ltd (China). Linden honey purchased from Fengzhichao Biological Engineering Co., Ltd (China). The 0.1 M phosphate buffer solution (PBS) was prepared by mixing 0.1 M NaH_2PO_4 and 0.1 M Na_2HPO_4 solutions in an appropriate ratio. All chemicals and reagents were analytical grade reagents and used as received without further purification.

2.2 Apparatus

The crystal structure of the prepared materials was characterized using a polycrystall X-ray diffractometer (XRD, X'pert3 Powder, PANalytical B.V., Alemlo, Netherlands) with Cu-Kα radiation ($\lambda = 1.5418$ Å) in the range of 5–90° with a scan step of $12° \text{ min}^{-1}$. The morphology and microstructure features were analyzed using scanning electron microscope (SEM, EVO 18, Zeiss, Oberkochen, Germany) and transmission electron microscope (TEM, JEM-2100, JEOL, Akishima-shi, Tokyo, Japan). Fourier transform infrared spectra (FT-IR) were performed using a Fourier Transform Infrared Spectrometer (Nicolet IS50, Thermo Fisher Scientific, Madison, USA) in the range of 4000–400 cm^{-1}.

Electrochemical properties, including cyclic voltammetry (CV) curves, differential pulse voltammetry (DPV) curves, and electrochemical impedance spectra (EIS), were performed using a CHI 660E electrochemical workstation (Shanghai Chenhua Instrument Co., Ltd, China) with a standard three-electrode cell. The prepared modified electrodes served as the working electrode, a platinum sheet electrode as the counter electrode and an Ag/AgCl electrode as the reference electrode. The electrolyte solution consisted of 0.1 M PBS (pH 7.0) solution containing 0.1 M KCl and 5 mM $[Fe(CN)_6]^{3-/4-}$. EIS measurements were performed in the frequency range of 0.1 Hz to 100 kHz. All the experiments were carried out at ambient temperature.

2.3 Synthesis of the (Cu-BTC)-MOF/Gr Composite

The preparation of the (Cu-BTC)-MOF/Gr Composite followed a two-step procedure (Scheme 1a). Firstly, the (Cu-BTC)-MOF was synthesized using a method reported previously with minor modification.[27] The detailed preparation process is shown in Scheme S1. The briefly, solution A was prepared by dissolving 0.004 mol of $Cu(NO_3)_2 \cdot 3H_2O$ and 0.004 mol of PVP K30 in 50 mL of methanol. Solution B was obtained by dissolving 0.002 mol of H_3BTC in 50 mL of methanol. Solution B was then slowly added into solution A by syringe. The mixture was aged at room temperature for 24 h, then centrifuged and washed three times with methanol and ethanol, respectively. The product was dried under vacuum at 60 °C for 12 h to obtain (Cu-BTC)-MOF.

Next, the (Cu-BTC)-MOF/Gr Composite was prepared. Appropriate amounts of (Cu-BTC)-MOF powder and graphene powder were dispersed in 20 mL of anhydrous ethanol under ultrasonication for 2 h. The resulting mixture was then washed three times with anhydrous ethanol and dried in a vacuum oven at 60 °C for 12 h to obtain (Cu-BTC)-MOF/Gr composite. Following this procedure, a series of (Cu-BTC)-MOF/Gr composites with different mass ratios of (Cu-BTC)-MOF to Gr (1 : 0.5, 1 : 0.75, 1 : 1, 1 : 1.25 and 1 : 1.5) were prepared. These composites were designated as (Cu-BTC)-MOF/Gr-1, (Cu-BTC)-MOF/Gr-2, (Cu-BTC)-MOF/Gr-3, (Cu-BTC)-MOF/Gr-4, and (Cu-BTC)-MOF/Gr-5, respectively.

2.4 Construction of the MIP/(Cu-BTC)-MOF/Gr/GCE electrochemical sensor

The construction of the MIP/(Cu-BTC)-MOF/Gr/GCE electrochemical sensor involved two steps. The detailed construction process is shown in Scheme 1b. First, the (Cu-BTC)-MOF/Gr/GCE modified electrode was constructed. The glassy carbon electrode (GCE, 3 mm diameter) was polished with 0.05 μm alumina slurry on a microcloth polishing pad, followed by sequential ultrasonicating in ultrapure water and anhydrous ethanol for 2 min each. This polishing-cleaning cycle was repeated until the redox peak potential difference in the cyclic voltammogram was less than 100 mV. The polished electrode was then dried at room temperature before use. A homogeneous suspension was prepared by dispersing appropriate amount of the (Cu-BTC)-MOF/Gr composite in 1 mL of IPA-deionized (DI) water (1 : 1, v/v) mixture under ultrasonication for 1 h. Subsequently, 5 μL of the suspension was dropped on the polished GCE and dried at room temperature. Then, 2 μL of the CHIT solution (0.5 wt%) was dropped on the modified surface. The (Cu-BTC)-MOF/Gr/GCE modified electrode was constructed after drying at room temperature.

In the second step, the MIP-CAP/(Cu-BTC)-MOF/Gr/GCE electrode was prepared. The detailed process is shown in Scheme S2. The as-prepared (Cu-BTC)-MOF/Gr/GCE electrode was immersed in 0.1 M PBS (pH 7.0) solution containing different content of CAP and *o*-PD. Subsequently, electropolymerization was performed by cyclic voltammetry between 0–0.8 V at a scan rate of 50 mV s^{-1} for different cycles. The MIP-CAP/(Cu-BTC)-MOF/Gr/GCE electrode was obtained after drying under ambient conditions. After that, the MIP-CAP/(Cu-BTC)-MOF/Gr/GCE electrode was separated by a magnet and washed with a methanol/acetic acid (9 : 1, v/v) solution under ultrasound, until complete removal of the CAP template molecules. Then the MIP/(Cu-BTC)-MOF/Gr/GCE electrochemical sensor was constructed after drying at room temperature. The non-imprinted polymer (NIP) control electrode was prepared following identical procedures, except for the absence of template molecules during the electropolymerization step.

2.5 Application of the as-prepared sensor on actual samples

The real samples used in this work were commercially available milk and honey, purchased from local supermarket, Guangzhou, China. The honey is moderately heated and then aspirated using a pipette. It is then mixed with PBS buffer solution at a volume ratio of 1 : 9, and ultrasonicated for 30 minutes to fully dissolve it. This treatment process can effectively reduce the viscosity of the honey samples, prevents interference to the detection results caused by uneven samples. The prepared MIP/(Cu-BTC)-MOF/Gr/GCE electrochemical sensor was applied to detect the CAP content of the above mixture employing the standard addition method. A 5 μL aliquot of the treated sample was dropped onto the prepared MIP/(Cu-BTC)-MOF/Gr/GCE electrochemical sensor, incubated for a period of time, and then analyzed *via* electrochemical methods.

3 Results and discussion

3.1 Structural and morphological characterization of as-prepared (Cu-BTC)-MOF/Gr composite

In this sensor, the as-prepared (Cu-BTC)-MOF/Gr composites were used as substrate material, guiding the orderly growth of MIP. The ratio of (Cu-BTC)-MOF to Gr is 1 : 1 in the (Cu-BTC-MOF/Gr composite. The microstructure and morphology of substrate materials are of vital importance. The as-prepared composites were characterized by several kinds of technology to confirm their microstructure and morphology. To investigate the phase composition and crystal structure, we performed XRD analysis on (Cu-BTC)-MOF, Gr, and the (Cu-BTC)-MOF/Gr composite. The XRD patterns are presented in Fig. 1. It can be seen that the XRD pattern of the synthesized (Cu-BTC)-MOF is similar to that of the simulated (Cu-BTC)-MOF (CCDC: 647646). The diffraction peaks of as-prepared (Cu-BTC)-MOF at 9.4°, 11.6°, and 19° are strong and sharp, corresponding to the (220), (222), and (440) crystal planes of (Cu-BTC)-MOF, respectively. The characteristic peaks of X-ray diffraction of Cu-BTC and the characteristic peaks of Cu-BTC reported can also match well.[27] It demonstrates that the highly crystalline (Cu-BTC)-MOF material was successfully synthesized. The diffraction peaks of Gr exhibits at 25° and 43.2°, corresponding to the (002) and (100) crystal planes. It also can be found from Fig. 1 that the diffraction peaks of the as-prepared (Cu-BTC)-MOF/Gr composite are identical with (Cu-BTC)-MOF and Gr materials and no new diffraction peaks appear. It indicates that the crystal structures of both (Cu-BTC)-MOF and Gr are preserved in the (Cu-BTC)-MOF/Gr composite. These results confirm that the microstructure of the (Cu-BTC)-MOF/Gr has not been damaged after composited with Gr and no impurities generate during the

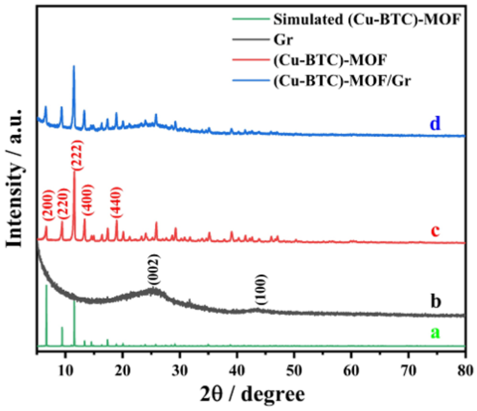

Fig. 1 XRD patterns of the (Cu-BTC)-MOF, Gr and Cu-BTC)-MOF/Gr composite.

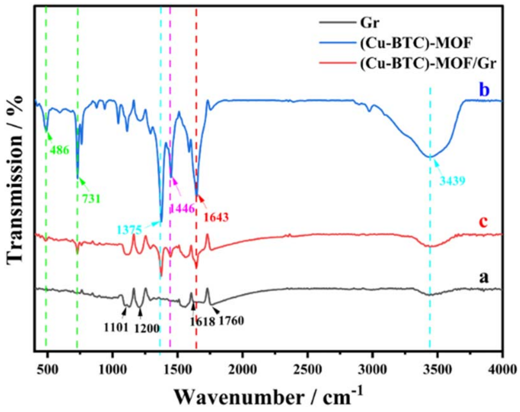

Fig. 2 FTIR spectra of (Cu-BTC)-MOF, Gr, and (Cu-BTC)-MOF/Gr composite.

preparation process. It demonstrates that the (Cu-BTC)-MOF/Gr material was successful formation.

Infrared spectroscopy elucidates the structural properties of prepared materials. FT-IR spectra of (Cu-BTC)-MOF, Gr, and (Cu-BTC)-MOF/Gr composite are showed in Fig. 2. As shown in the figure, Gr exhibits a weak stretching vibration peak of –OH at 3439 cm^{-1}. The peaks at 1101 cm^{-1} and 1760 cm^{-1} in Gr related to the weak stretching bands of C=O and –COOH, while the characteristic peaks at 1200 cm^{-1} and 1618 cm^{-1} correspond to the stretching vibration and bending vibration of C–OH, respectively. For (Cu-BTC)-MOF material, the peaks at 3439 cm^{-1} and 1375 cm^{-1} associate with absorption peaks of stretching vibration and in-plane deformation vibration of –OH, which coming from the characteristic absorption of organic ligands. The stretching vibration absorption peak at 1643 cm^{-1} represents the –COOH characteristic peak. The peak at 1446 cm^{-1} corresponds to the stretching vibration of the –C=C bond of the benzene ring, while those at 731 cm^{-1} and 486 cm^{-1} are contributed to the tensile and bending vibrations of Cu–O. These characteristic peaks indicate the successful synthesis of (Cu-BTC)-MOF. Furthermore, the characteristic absorption peaks of both (Cu-BTC)-MOF and Gr are clearly visible in the (Cu-BTC)-MOF/Gr composite, though the intensity is slightly diminished. This indicates that the (Cu-BTC)-MOF/Gr composite material was success.

For molecularly imprinted electrochemical sensors, the substrate material can increase the specific surface area of the electrode, allowing more MIP sites to be fixed. It can also enhance the electronic conductivity and strengthen the chemical signal of the electrode. These characteristics are beneficial to improving the detection capacity of the sensor. Therefore, the properties of the substrate material, such as particle size and controlled morphology are crucial for the performance of sensors.[37] The microscopic morphologies of the synthesized materials were characterized by SEM. As displayed in Fig. S1a, the morphologies of (Cu-BTC)-MOF crystals are a well-defined octahedral morphology with uniform particle size distribution. Its particle size is about 500–600 nm and the crystal surfaces display micropores. Fig. S1b–f show the SEM images of (Cu-BTC)-MOF/Gr composites with varying mass ratios of (Cu-BTC)-MOF and graphene. From the images of Fig. S1b–f, it can be found that the graphene matrix clearly exhibits characteristic layered structures. The (Cu-BTC)-MOF crystals maintain their original octahedral morphology in the (Cu-BTC)-MOF/Gr composite. It indicates that the microstructures of the (Cu-BTC)-MOF and Gr were not damaged during the compounding process. It also shows that the (Cu-BTC)-MOF particles are uniformly distributed on the graphene sheets. Notably, as the mass ratio of (Cu-BTC)-MOF to Gr decreases, the density of (Cu-BTC)-MOF crystals anchored on compositions decreases. The (Cu-BTC)-MOF/Gr composite materials prepared under 1 : 1 mass ration of (Cu-BTC)-MOF to Gr, are suitable for constructing the MIP sensors.

To further investigate the microscopic morphology of the synthesized materials, transmission electron microscopy analysis was conducted on (Cu-BTC)-MOF, graphene, and the (Cu-BTC)-MOF/Gr composite. Fig. 3 displays the TEM images of these materials. As revealed in Fig. 3a, the (Cu-BTC)-MOF crystals exhibit well-defined octahedral morphology with sharp edges and particle size of approximately 600 nm. Fig. 3b clearly demonstrates the characteristic ultrathin sheet-like structure of graphene. Most significantly, Fig. 3c shows that the octahedral (Cu-BTC)-MOF crystals are successfully anchored onto the graphene sheets *via* strong van der Waals interactions, confirming

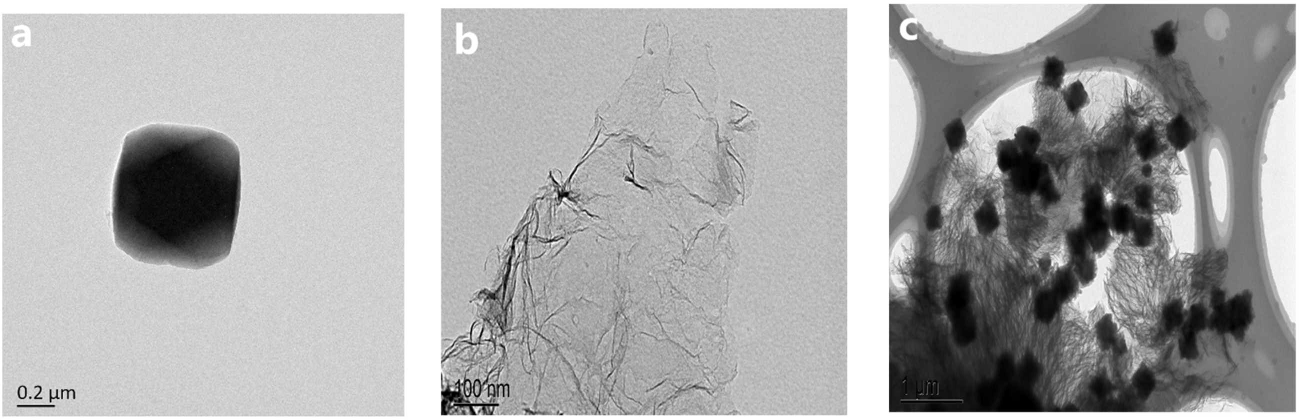

Fig. 3 TEM images of as-prepared materials: (a) (Cu-BTC)-MOF, (b) Gr, (c) (Cu-BTC)-MOF/Gr (1 : 1 ratio of (Cu-BTC)-MOF to Gr).

the successful preparation of the (Cu-BTC)-MOF/Gr composite. These results identify with the previous report.[27]

3.2 Electrochemical properties of the different modified electrodes

To investigate the influence of the composition of modified electrodes on their electrochemical performance, CV experiments were employed to study the electrochemical behavior of different modified electrodes in a 0.1 M PBS (pH 7.0) solution containing 5 mM $[Fe(CN)_6]^{3-/4-}$ redox pair and 0.1 M KCl at scan rate of 50 mV s^{-1}. Fig. 4a displays the CV curves of various modified electrodes. The CV peak currents of different modified electrodes are shown in Table S1. From Fig. 4a and Table S1, it can be found that the bare GCE electrode exhibits a pair of well-defined redox peaks in the $[Fe(CN)_6]^{3-/4-}$ solution (black line), with an oxidation peak current of 85.3 μA. After decorated by (Cu-BTC)-MOF, the oxidation peak current of the (Cu-BTC)-MOF/GCE modified electrode decreases to 42.4 μA due to the poor conductivity of (Cu-BTC)-MOF (red line). When the GCE electrode is modified with graphene (Gr), the resulting Gr/GCE modified electrode exhibits a substantial increase in the oxidation peak current, reaching 216.0 μA (blue line). This indicates that the highly conductive graphene significantly enhances the electrochemical signal. Compared to the (Cu-BTC)-MOF/GCE modified electrode, the (Cu-BTC)-MOF/Gr/GCE modified electrode, decorated by the highly conductive (Cu-BTC)-MOF/Gr composite, exhibits a higher current response signal of 117 μA (green line). After the electropolymerization of MIP and CAP on the (Cu-BTC)-MOF/Gr/GCE modified electrode, the oxidation peak current of the MIP-CAP/(Cu-BTC)-MOF/Gr/GCE modified electrode sharply decreases to 31.6 μA due to the poor conductivity of the molecularly imprinted film containing *o*-PD and CAP (light blue line). Following elution, the oxidation peak current of the MIP/(Cu-BTC)-MOF/Gr/GCE recovers to 71.6 μA as a result of the removal of the template molecules (pink line). In contrast, the NIP/(Cu-BTC)-MOF/Gr/GCE, which was prepared without the template molecule, still shows a very small oxidation peak current of 18.2 μA after elution (brown line).

To further investigate the electrochemical properties of the as-prepared modified electrodes, the EIS of the fabricated modified electrodes were conducted. The Nyquist plots of the fabricated different modified electrodes are presented in Fig. 4b. The insert of Fig. 4b is the partial enlarged detail. The semi-circle diameter in the high-frequency region of the Nyquist curve refer to the electron transfer resistance (R_{ct}) of the modified electrode, which is related to the electron transfer kinetics for the redox probe on the surface of electrode. R_s represents the solution ohmic resistance. The fitted results of Nyquist plots display in Table S2. As shown in Fig. 4b, the values of the electron transfer resistance for all the modified electrodes except the Gr/GCE and (Cu-BTC)-MOF/Gr/GCE modified electrodes are larger than that of bare GCE electrode in the $[Fe(CN)_6]^{3-/4-}$ solution. The R_{ct} value of the bare GCE electrode is 297.6 Ω. After modified with Gr, the R_{ct} value of the Gr/GCE modified electrode decrease to 55.92 Ω owing to the high conductivity of Gr. Compared to the bare GCE electrode, the R_{ct} values increase to 1897, 3433 and 908.3 Ω for (Cu-BTC)-MOF/GCE, MIP-CAP/(Cu-BTC)-MOF/Gr/GCE and the MIP/(Cu-BTC)-MOF/Gr/GCE electrode (Table S2), respectively. The reason is that non-conductivity (Cu-BTC)-MOF, molecularly imprinted film and GAP hinder the electron transfer in modified electrode and results in the increase of R_{ct} values. It is worth noting that the electron transfer resistance of the (Cu-BTC)-MOF/Gr/GCE modified electrode (274.5 Ω) is significantly lower than that of the (Cu-BTC)-MOF/GCE electrode (1897 Ω) because the excellent conductivity of Gr in (Cu-BTC)-MOF/Gr composite promotes the electron transfer in modified electrode. After the electropolymerization of MIP and CAP on the (Cu-BTC)-MOF/Gr/GCE modified electrode, the R_{ct} of the MIP-CAP/(Cu-BTC)-MOF/Gr/GCE modified electrode increased to 3433 Ω due to the poor conductivity of the molecularly imprinted film containing *o*-PD and CAP. Significantly, after elution, the R_{ct} value of the MIP/(Cu-BTC)-MOF/Gr/GCE electrode decreases to 908.3 Ω because

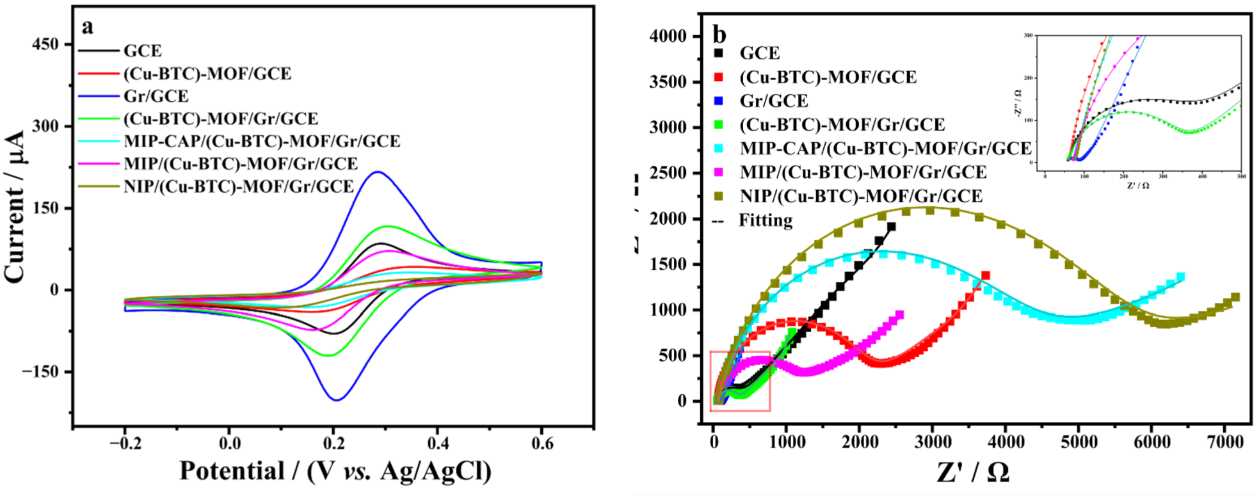

Fig. 4 Electrochemical properties of different modified electrodes: (a) CV curves, (b) Nyquist plots, insert is the partial enlarged detail.

of the removal of the template molecules. In contrast, the NIP/(Cu-BTC)-MOF/Gr/GCE, prepared without template molecules, exhibits the highest R_{ct} value of 4552 Ω after elution. The EIS results are consistent with the previous results of CV data (Fig. 4a). The results of the electrochemical analysis demonstrate that (Cu-BTC)-MOF/Gr composite is helpful to enhance the response signal of modified electrode.

In order to further confirm the contribution of (Cu-BTC)-MOF and Gr in the sensor, we conduct electrochemical performance tests on three electrodes prepared using different substrate materials. The test results are shown in Fig. S2, Tables S1 and S2. From the CV curves (Fig. S2a) and EIS (Fig. S2b) test results, it can be seen that compared with the MIP/GCE sensor, the sensors modified with (Cu-BTC)-MOF, Gr and (Cu-BTC)-MOF/Gr composite have higher response current and lower electron transfer resistance. Among them, the electrode modified with (Cu-BTC)-MOF/Gr composite material possesses the highest redox peak current (71.6 μA) and the lowest charge transfer impedance (908.3 Ω), which directly proves its optimization effect on the electrochemical performance.

3.3 Electrochemical behaviour of the fabricated electrochemical sensor toward CAP

In order to determine the electrocatalytic activity and stability of the MIP/(Cu-BTC)-MOF/Gr/GCE molecularly imprinted electrochemical sensor toward CAP, the electrochemical behaviors of the sensors including MIP/GCE, MIP/(Cu-BTC)-MOF/GCE, MIP/Gr/GCE and MIP/(Cu-BTC)-MOF/Gr/GCE sensor were studied using DPV method before and after incubating CAP. The CAP incubation was carried out in a 100 μM CAP solution at 37 °C for 30 minutes. The investigation was conducted in a 0.1 M PBS (pH 7.0) solution containing 5 mM $[Fe(CN)_6]^{3-/4-}$ redox pair and 0.1 M KCl. The results are showed in Fig. 5. It can be found that the response currents of all sensors decrease sharply after re-incubation with CAP. The difference in response currents before and after incubation with CAP can declare the sensing abilities of the sensor for CAP. The greater the difference, the better sensing abilities. The difference of response currents for the MIP/(Cu-BTC)-MOF/Gr/GCE sensor is biggest before CAP incubation (black dash line) and after re-incubation with CAP (black solid line), followed by the MIP/Gr/GCE (red line) and MIP/(Cu-BTC)-MOF/GCE (blue line) sensors, and the that of the MIP/GCE (green line) sensor is the smallest. For the NIP/(Cu-BTC)-MOF/Gr/GCE modified electrode, the current is low before CAP incubation (pink dash line) and there are no obvious current signals change after ACP incubation (pink solid line). These results demonstrate that the (Cu-BTC)-MOF/Gr composite materials play a significant role in enhancing the sensing properties of the molecular imprinting sensors. It also indicates that the MIP/(Cu-BTC)-MOF/Gr/GCE molecularly imprinted electrochemical sensor can effectively detect CAP.

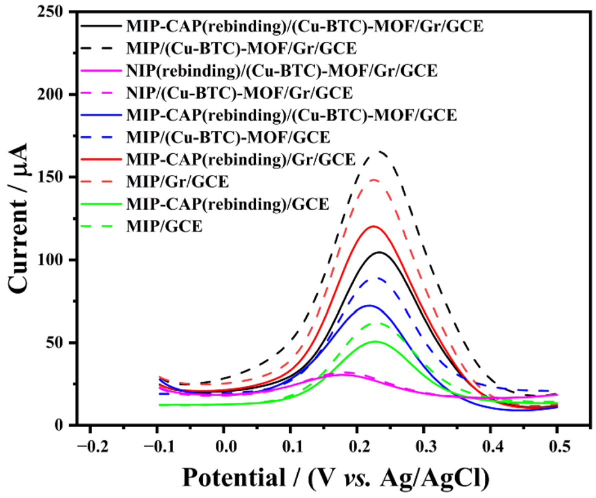

Fig. 5 DPV curves of as-prepared sensors before incubation and after incubation of CAP.

In order to investigate the electrochemical behaviors of the prepared MIP/(Cu-BTC)-MOF/Gr/GCE sensor, the CV was employed in a PBS (pH 7.0) buffer solution containing the $[Fe(CN)_6]^{3-/4-}$ redox pair under different scan rates from 25 to 200 mV s^{-1} on the MIP/(Cu-BTC)-MOF/Gr/GCE sensor after CAP incubation. The results are shown in Fig. S3. As shown in Fig. S3a, the redox currents of the CAP-incubated MIP/(Cu-BTC)-MOF/Gr/GCE sensor increase with the increase of the scan rates. Furthermore, Fig. S3b reveals that both the oxidation peak current and reduction peak current exhibited good linear relationships with the square root of the scan rate. This indicates that the electrochemical reaction process on the surface of this molecularly imprinted electrochemical sensor is typically diffusion-controlled. The corresponding regression equations are as follows:

$$I_{pa}(\mu A) = 7.098v^{1/2} - 6.086\ (R^2 = 0.9994) \quad (1)$$

$$I_{pc}(\mu A) = -9.939v^{1/2} + 20.862\ (R^2 = 0.9985) \quad (2)$$

3.4 Optimization experimental parameters of the sensor based on (Cu-BTC)-MOF/Gr composite

To improve the performance of the MIP/(Cu-BTC)-MOF/Gr/GCE sensor for CAP detection, the constructed parameters of the MIP/(Cu-BTC)-MOF/Gr/GCE sensor were optimized by DPV method in a 0.1 M PBS (pH = 7.0) solution containing 5 mM $[Fe(CN)_6]^{3-/4-}$ redox pair and 0.1 M KCl. During optimization process, all parameters were kept invariable except the parameter under study. The constructed parameters include the proportion of (Cu-BTC)-MOF to Gr, (Cu-BTC)-MOF/Gr concentration, proportion of CAP to *o*-PD in the electropolymerization solution, number of electropolymerization cycles, elution time, and incubation time. The experimental results are showed in Fig. S4. Among these parameters, the optimal incubation time was determined based on the difference in DPV current before and after CAP incubation, while the remaining experimental conditions were optimized by comparing the DPV current before and after elution.

The proportion of (Cu-BTC)-MOF to Gr has a significant impact on the specific surface area, morphology and conductivity of the (Cu-BTC)-MOF/Gr composite. Insufficient Gr leads to excessively the low conductivity of the composite, while excessive graphene causes agglomeration. This agglomeration reduces specific surface area of the composite and decreases the number of available MIP sites. Therefore, the proportion of (Cu-BTC)-MOF to Gr in (Cu-BTC)-MOF/Gr composite was firstly studied. As shown in Fig. S4a, the current in DPV for the prepared MIP/(Cu-BTC)-MOF/Gr/GCE sensor gradually goes up with increasing Gr content and reaches a highest value when the mass ratio of (Cu-BTC)-MOF to Gr is 1 : 1. After that, the current decreases. Thus, a 1 : 1 ratio of (Cu-BTC)-MOF to Gr was selected for the (Cu-BTC)-MOF/Gr composite used to construct the sensor in this work.

The (Cu-BTC)-MOF/Gr composite serves as a substrate material for the molecularly imprinted electrochemical sensor. It provides excellent conductivity and a large specific surface area, both of which influence the polymerization effect of the molecularly imprinted polymer. Therefore, the loading content of (Cu-BTC)-MOF/Gr composite on the modified electrode has a significant impact on the sensor performance. Fig. S4b shows the relationship between the (Cu-BTC)-MOF/Gr composite concentration and the response currents of the sensor. It can be seen that the response current increases with the rising of composite concentration, reaching a maximum value at 1 mg mL^{-1}, after which it decreases. Therefore, the (Cu-BTC)-MOF/Gr composite concentration of 1 mg mL^{-1} was used in further experiments.

The molar proportion of template molecule to functional monomer is directly related to the number of active recognition sites in the final MIP. As shown in Fig. S4c, at a low ratio, the insufficient number of functional monomers limits the ability of template molecules to effectively combine and crosslink with them, leading to the formation of molecularly imprinted membranes with few effective recognition sites. This results in minimal current change before and after elution. As the number of functional monomers gradually increases, more template molecules can combine with the functional monomers. The number of imprinted cavities formed in the polymer increases, leading to a larger current difference before and after elution. It achieves its maximum at a ratio of 1 : 5. Subsequently, as the number of functional monomers further increases, the excess monomers cause MIP to undergo self-polymerization. This makes it difficult to elute the template monomers, resulting in a smaller current difference before and after elution. Hence, the molar proportion of template molecule to functional monomer was chosen to use 1 : 5 in following experiments.

The electropolymerization process of molecularly imprinted membrane was performed by cyclic voltammetry method between 0–0.8 V at a scan rate of 50 mV s^{-1}. The number of electropolymerization cycles is directly related to the thickness of the MIP film. As shown in Fig. S4d, before 20 cycles, the magnitude of DPV current change gradually increases because the rise in the number of electropolymerization cycles facilitates MIP formation. When the number of polymerization cycles reaches 20, the current response peaks. Subsequently, as the number of cycles further increases, the excessive thickness of the MIP film hinders the elution of template molecules, leading to a decrease in the magnitude of the current change. The final determination for the number of scanning cycles in the molecularly imprinted membrane polymerization is 20 cycles.

Following electropolymerization, elution is necessary to remove the template molecules and form recognition sites for CAP binding. Thus, selecting an appropriate elution time is crucial. As illustrated in Fig. S4e, prior to 20 min, the difference of current response before and after elution gradually increases with prolonged elution time. It indicates gradual removal of the template molecules, with the maximum response achieved at 20 minutes. Beyond 20 minutes, the current response no longer increases, suggesting that the elution process is complete by this time. Therefore, the elution time was set at 20 minutes in the following experiments.

To determine the optimal incubation time, the prepared MIP/(Cu-BTC)-MOF/Gr/GCE sensor was incubated with CAP. As shown in Fig. S4f, the difference of DPV current response before and after incubation reaches its maximum at 30 minutes, indicating that the incubation process reaches saturation by

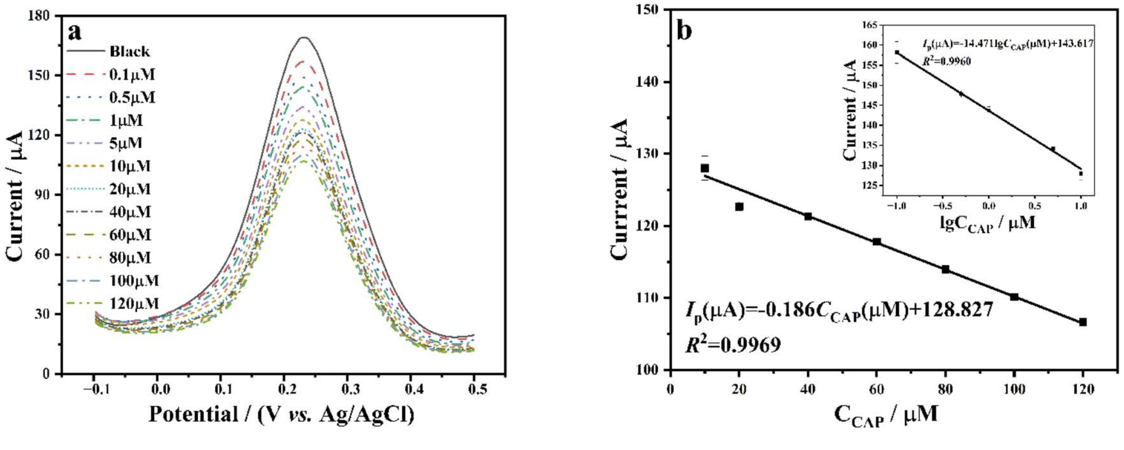

Fig. 6 (a) Current response of MIP/(Cu-BTC)-MOF/Gr/GCE sensor for different concentrations of CAP in 0.1 M PBS (pH 7.0) solution. (b) Linear relationship between response current and CAP concentration, insert is linear relationship between response current and the logarithm of CAP concentration at low concentrations.

this point. Finally, the optimal incubation time was set to 30 minutes for the subsequent experiment.

3.5 Analytical performance of the fabricated molecularly imprinted electrochemical sensor

The linear range of the MIP/(Cu-BTC)-MOF/Gr/GCE electrochemical sensor to CAP which fabricated under optimal conditions was determined by DPV measurement in a 0.1 M PBS (pH = 7.0) solution containing 5 mM $[Fe(CN)_6]^{3-/4-}$ redox pair and 0.1 M KCl. As it can be seen at Fig. 6a, the response currents of the sensor gradually decreased with increasing CAP concentration. Fig. 6b demonstrates a good linear relationship between the response current and the logarithm of CAP concentration within the range of 0.1 to 10 μM. The linear regression equation is $I_p(\mu A) = -14.471 \lg C_{CAP}(\mu M) + 143.617$, with a correlation coefficient of $R^2 = 0.9960$ (insert in Fig. 6b). Here, I and C correspond to the response current and CAP concentration, respectively. Furthermore, Fig. 6b also reveals an excellent linear correlation between response current and CAP concentration in the range of 10 to 120 μM, represented by regression curve as: $I_p(\mu A) = -0.186C_{CAP}(\mu M) + 128.827$ with a correlation coefficient of $R^2 = 0.9969$. Based on a signal-to-noise ratio (S/N) of 3, the low limit of detection (LOD) is determined to be 0.05 μM. The sensor possesses a high sensitivity of 0.186 μA μM^{-1}. At the range of 0.1 to 10 μM, the dependence on the logarithm of CAP concentration indicates a sensitivity that exceeded the normal low detection limit. The performance of this chloramphenicol sensor was compared with several electrochemically-based CAP sensors reported in the literature, as summarized in Table 1. The comparative results demonstrate that the prepared MIP/(Cu-BTC)-MOF/Gr/GCE electrochemical sensor exhibits both a wider detection range and a lower detection limit (LOD) than most previously reported systems.

3.6 Selectivity, reproducibility and stability of the sensor based on the (Cu-BTC)-MOF/Gr composite

The selectivity of the electrochemical sensor is a crucial characteristic, enabling the specific recognition of the target substrate in real samples. According to several common antibiotics, the influence of 1 μM oxytetracycline (OTC), 1 μM gentamicin sulfate (GM), 1 μM streptomycin sulfate (SS), 1 μM neomycin sulfate (NS) and 1 μM tetracycline (TC) on the response current of the fabricated MIP/(Cu-BTC)-MOF/Gr/GCE sensor were investigated by DPV in a 0.1 M PBS (pH 7.0) solution containing 5 mM $[Fe(CN)_6]^{3-/4-}$ redox pair and 0.1 M KCl. From Fig. 7a, it can be seen that the interfering antibiotics did not induce significant current changes when compared to pure CAP and mixed standards. These results demonstrate that these

Table 1 Performance of the MIP/(Cu-BTC)-MOF/Gr/GCE electrochemical sensor compared with those reported CAP sensors in literatures[a]

Sensor	Methods	Linear range/μM	LOD/μm	References
MoS_2/PANI/CPE	DPV	0.1–100	0.069	38
MoS_2/2D rGO/GCE	DPV	5–35	1	39
rGO/PdNPs/GCE	DPV	0.05–1	0.05	40
3D CNTs/CuNPs/MIP	CV	10–500	10	41
N-G/AuNPs/GCE	LSV	2–80	0.59	42
rGO@PDA@AuNPs	DPV	0.1–100	0.058	10
MIP/(Cu-BTC)-MOF/Gr/GCE	DPV	0.1–120	0.05	This work

[a] PANI: polyaniline; CNTs: carbon tubes; GCE: glassy carbon electrode; rGO: reduced graphene oxide; CPE: carbon paste electrode; PdNPs: Pd nano particles; CuNPs: Cu nano particles; Au NPs:Au nano particles; PDA: polydopamine.

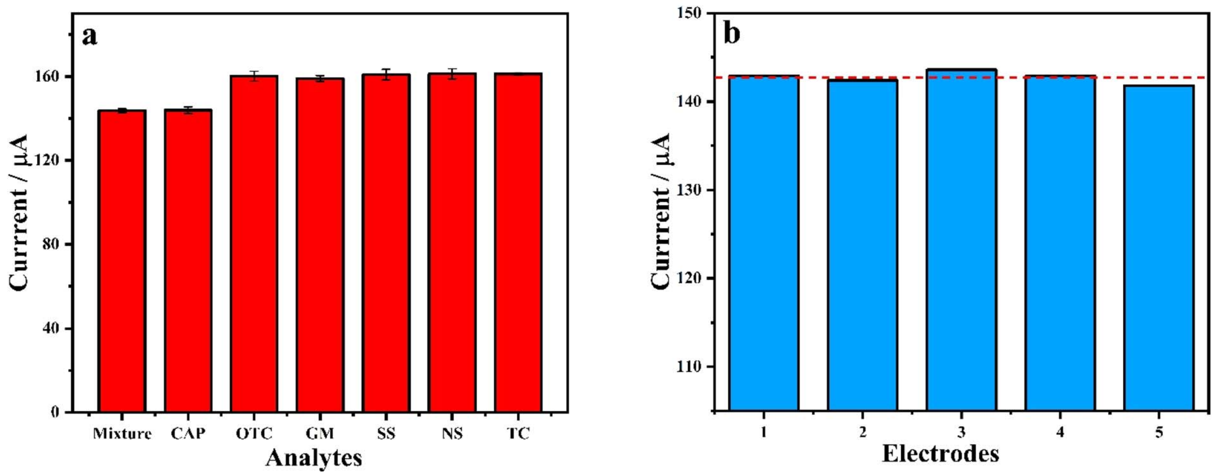

Fig. 7 The selectivity and reproducibility of MIP/(Cu-BTC)-MOF/Gr/GCE sensor: (a) effect of interferents, (b) reproducibility study.

Table 2 Recovery for the determination of CAP in milk and honey ($n = 3$)

Samples	Added (μM)	Detected (μM)	Recovery (%)	RSD (%)
Milk	1	1.11 ± 0.11	111.24	9.50
	100	100.05 ± 0.62	100.50	0.62
Honey	1	1.08 ± 0.07	94.88	6.31
	100	100.86 ± 0.62	95.60	0.62

potential interferents have negligible effects on CAP detection, indicating the excellent anti-interference capability of the as-prepared sensor. The reproducibility was also evaluated using five batches of the MIP/(Cu-BTC)-MOF/Gr/GCE electrochemical sensors prepared under the optimal conditions for CAP detection. The evaluation was conducted in a 0.1 M PBS (pH 7.0) solution containing 5 mM $[Fe(CN)_6]^{3-/4-}$ redox pair and 0.1 M KCl. The relative standard deviation (RSD) of the measurements is 0.47% (Fig. 7b), demonstrating an excellent reproducibility for the fabricated sensor.

To assess the stability of the MIP/(Cu-BTC)-MOF/Gr/GCE sensor, it underwent 50 consecutive CV cycles. As shown in Fig. S5a, after 50 CV cycles, the response currents decrease from 66.8 μA to 66.3 μA, corresponding to a current retention rate of 99.25%. To further confirm the long-term stability of the sensor, the DPV response currents retention rates were monitored over storageperiods of different days at 4 °C (Fig. S5b). Notably, after 21 days of storage, the sensor retained 85.09% of its initial current response, indicating excellent long-term stability.

3.7 Application of the fabricated sensor on actual food samples

To further evaluate the performance of the fabricated MIP/(Cu-BTC)-MOF/Gr/GCE electrochemical sensor in actual food sample detection, standard addition recovery experiments were performed for CAP detection in milk and honey (purchased from local supermarket). The milk and honey were dissolved in a PBS (pH 7.0) solution. The CAP standard solution of two different concentrations (1 and 100 μM) was spiked into the diluted milk and honey samples and tested by CV method. As shown in Table 2, the recoveries range from 100.50% to 111.24% for milk and 94.88% to 95.60% for honey. And RSD ($n = 3$) values are below 9.50% and 6.31% for milk and honey samples, respectively. These results demonstrate that the as-prepared molecularly imprinted electrochemical sensor based on (Cu-BTC)-MOF and graphene composite is a promising and reliable tool for the sensitive and rapid CAP quantification in actual food samples.

4 Conclusions

In summary, a sensitive and selective molecularly imprinted electrochemical sensor was constructed based on (Cu-BTC)-MOF and graphene composite for CAP detection. In this work, the layered cross structure (Cu-BTC)-MOF/Gr composites served as a substrate material for the sensor significantly improved the active recognition sites in MIP, enhanced the electronic conductivity and strengthen the chemical signal of the sensor. *o*-PD served as a functional monomer with two amino active sites, which enable hydrogen bonding or electrostatic interactions with functional groups of target molecules, thus enhancing template-specific recognition. These characteristics are beneficial to improving the detection capacity of the sensor. The constructed (Cu-BTC)-MOF/Gr based sensor demonstrated an excellent wide dynamic response range for CAP molecules, featuring a high sensitivity of 0.186 μA μM^{-1} and low limit of detection of 0.05 μM within a broad linear sensing range of 0.1–100 μM. At the range of 0.1 to 10 μM, the dependence on the logarithm of CAP concentration indicated a sensitivity that exceeded the normal low detection limit. Moreover, the (Cu-BTC)-MOF/Gr based sensor exhibited high reproducibility, excellent selectivity against similar interferents and good stability, making it highly promising for efficient CAP monitoring. The constructed electrochemical molecularly imprinted sensor enables accurate detection of CAP in some

CAP-containing food samples including milk, meat, honey and so on. Overall, the sensor based on (Cu-BTC)-MOF/Gr composite and *o*-PD functional monomer indicates that the rational design of nanocomposites with high specific surface area and conductivity, combined with the selection of suitable functional monomers, can significantly enhance the detection performance and selectivity of molecularly imprinted sensors. The MIP/(Cu-BTC)-MOF/Gr/GCE electrochemical sensor developed in this study is simple to use and can serve as a sensitive platform for the electrochemical sensing of CAP. It can be applied for the detection of CAP in various actual food.

Author contributions

J. H. P.: conceptualization, methodology, experimental data production, analysis of the obtained results, and preparation of manuscript material. S. J. Q.: validation, formal analysis, investigation, data curation, writing – original draft preparation, N. X.; conceptualization, methodology, analysis, and generalization of the obtained results, writing of the original manuscript. J. P.: project administration, funding acquisition. All authors have read and agreed to the published version of the manuscript.

Conflicts of interest

There are no conflicts to declare.

Data availability

The data supporting the findings of this study are available within the article and in the supplementary information (SI). Supplementary information is available. See DOI: https://doi.org/10.1039/d5ra10071b.

Acknowledgements

This work was funded by the National Natural Science Foundation of China (No. 22278152, 22478131).

Notes and references

1 Y. Liu, K. Yan, O. K. Okoth and J. D. Zhang, *Biosens. Bioelectron.*, 2015, **74**, 1016.

2 G. M. Yang and F. Q. Zhao, *Biosens. Bioelectron.*, 2015, **64**, 416.

3 X. H. Liang, X. Y. Fang, Y. C. Yang, J. F. Li, H. J. Liu and L. Y. Wang, *Luminescence*, 2016, **31**, 168.

4 X. F. Qin, Q. Q. Wang, L. P. Geng, X. L. Shu and Y. Wang, *Talanta*, 2019, **197**, 28.

5 Q. H. Wang, X. D. Qi, H. Y. Chen, J. G. Li, M. Yang, J. Liu, K. Sun, Z. H. Li and G. W. Deng, *Microchim. Acta*, 2022, **189**, 272.

6 L. R. Guidi, P. A. S. Tette, C. Fernandes, L. H. M. Silva and M. B. A. Gloria, *Talanta*, 2016, **70162**, 324.

7 A. Gantverg, I. Shishani and M. Hoffman, *Anal. Chim. Acta*, 2003, **483**, 125.

8 X. Y. Pei, N. Zhang, Y. T. Chen, S. Y. Mial, H. Y. Fu, Q. Q. Zhu, Z. B. Dai, Y. Chi, L. G. Hu and R. Jin, *Microchem. J.*, 2025, **212**, 113198.

9 A. A. Boane, R. G. Rocha, R. A. A. Muñoz, A. L. D. Santos and E. M. Richter, *Electrochim. Acta*, 2025, **526**, 146175.

10 L. Zhang, M. Yin, X. X. Wei, Y. W. Sun, Y. Chen, S. Y. Qi, X. X. Tian, J. X. Qiu and D. P. Xu, *Diam. Relat. Mater.*, 2022, **128**, 109311.

11 X. Qi, Z. X. Teng, J. H. Yu, D. L. Jia, Y. F. Zhang and H. Z. Pan, *Mater. Lett.*, 2023, **330**, 133350.

12 S. Liu, G. S. Lai, H. L. Zhang and A. M. Yu, *Microchim, Acta*, 2017, **184**, 1445.

13 Y. X. Li, L. X. Luo, Y. Q. Kong, Y. J. Li, Q. S. Wang, M. Q. Wang, Y. Li, A. Davenport and B. Li, *Biosens. Bioelectron.*, 2024, **294**, 116018.

14 J. Wang, Z. N. Zhang, X. R. Gao, H. T. Han, S. R. Guo, Y. L. Zhai, R. Y. Yuan, X. X. Wang and M. S. He, *Talanta*, 2025, **292**, 127949.

15 A. B. Hashkavayi, A. Alizadeh, R. Azimi, M. Peyrovi, J. B. Raoof and H. G. Chun, *Heliyon*, 2023, **9**, e17169.

16 A. M. El-Kosasy, A. H. Kamel, L. A. Hussin, M. F. Ayad and N. V. Fares, *Food Chem.*, 2018, **250**, 188.

17 L. Wu, H. Yan, G. H. Li, X. Xu, L. Zhu, X. Q. Chen and J. Wang, *Food Anal. Methods*, 2019, **12**, 1648.

18 R. Nie, D. Y. Liao, W. J. Yan, W. T. Liang, J. H. Zhi, Y. J. Guo, C. Dong and L. F. Fan, *Sensor. Actuat. B-Chem.*, 2025, **430**, 137357.

19 A. Cetinkaya, S. Bilge., L. Karadurmus, A. Sınag and S. A. Ozkan, *Tren. Anal. Chem.*, 2022, **147**, 116512.

20 L. H. Ding, Y. W. Wang, Q. W. Li, L. L. Zhang and A. Z. Wang, *Rare Met*, 2024, **43**(9), 1909.

21 W. J. Li, Y. E. Zhong, P. Zhou, P. P. Li, S. Huang, X. H. Zhu, Y. Y. Zhang, M. L. Liu and S. Z. Yao, *Talanta*, 2025, **294**, 128278.

22 I. Chandio, S. Rahujo, Z. A. Chandio, M. A. Rashid, M. U. Rehman, Z. H. Shar and K. H. Thebo, *Bioelectrochemistry*, 2025, **165**, 109006.

23 S. T. Liu, Z. Y. Zengcai, J. Y. Yang, T. H. Wang, W. T. Lin, Y. H. Pi and T. J. Wang, *Appl. Catal. B-Environ. Energy*, 2025, **374**, 125376.

24 R. Y. Cong, K. Y. Hu, D. D. Hu, J. R. Sun, J. L. Yao, Z. Y. Guo, S. Wang and Y. F. Hu, *Microchem. J.*, 2025, **212**, 113236.

25 P. Gao, M. Z. Hussain, D. Gryc, S. Mukherjee, Z. Y. Zhou, W. J. Li, A. Jentys, M. Elsner and R. A. Fischer, *Biosens. Bioelectron.*, 2025, **286**, 117598.

26 L. L. Li, D. D. Lei, P. Y. Song, Q. B. Xu, L. H. Huang, X. Ma, L. D. Zhou, P. Zhang and W. J. Kong, *Analyst*, 2026, **151**(3), 749.

27 S. Wang, Y. Q. Yao, J. Zhao, X. H. Han, C. P. Chai and P. Dai, *Rsc Adv.*, 2022, **12**, 5164.

28 K. Kaewpradub, K. Veenuttranon, H. Jantapaso, P. Mittraparp-arthorn and I. Jeerapan, *Nano-micro. Lett.*, 2025, **17**, 71.

29 L. Shi, J. Song, Y. Wang, H. Fu, K. Patrick-Iwuanyanwu, L. Zhang, C. H. Lawrie and J. H. Zhang, *Nano-micro. Lett.*, 2025, **17**, 246.

30 Y. Q. Ma and H. J. Ahn, *Sci. Technol. Adv. Mat.*, 2025, **26**, 2459051.

31 P. W. Liang, D. Pan, X. Hu, K. R. Yang, Y. J. Liu, Z. J. Huo, Z. Bo, L. H. Xu, J. H. Xu and Z. H. Wen, *Nano-micro. Lett.*, 2025, **17**, 237.

32 A. I. Mugisha, C. Fauteux-Lefebvre, P. Thangarasu and C. A. Huerta-Aguilar, *J. Mol. Struct.*, 2025, **1339**, 142382.

33 Y. X. Diao, G. X. Hu, S. Cui, Y. Shi, H. D. Wang and Z. Li, *Bioresource Technol.*, 2025, **429**, 132512.

34 C. Awada, H. H. Hammud, W. A. Aljamhi, S. Boscarino, A. Scandurra and F. Ruffino, *Appl. Surf. Sci.*, 2025, **706**, 163588.

35 T. Lin and J. Z. Li, *Acs Appl. Electron. Mater.*, 2025, **7**, 5153.

36 J. Y. Sun, K. J. Huang, S. Y. Wei, Z. W. Wu and F. P. Ren, *Colloid. Surfaces B*, 2011, **84**, 421.

37 M. D. Mukendi, O. S. Salami and N. Mketo, *Micromachines*, 2025, **16**, 251.

38 T. Yang, H. Y. Chen, T. Ge, J. Wang, W. H. Li and K. Jiao, *Talanta*, 2015, **144**, 1324.

39 N. X. Dinh, T. N. Pham, T. Q. Huy, D. Q. Trung, P. A. Tuan, V. Q. Khue, N. V. Quy, V. P. Le, V. D. Lam and A. T. Le, *New J. Chem.*, 2021, **45**, 7622.

40 W. W. Yi, Z. P. Lia, C. Dong, H. W Li and J. F. Li, *Microchem. J.*, 2019, **148**, 774.

41 A. Munawar, M. A. Tahir, A. Shaheen, P. A. Lieberzeit, W. S. Khan and S. Z. Bajwa, *J. Hazard. Mater.*, 2018, **342**, 96.

42 J. Borowiec, R. Wang, L. H. Zhu and J. D Zhang, *Electrochim. Acta*, 2013, **99**, 138.